Acta Geotechnica
https://doi.org/10.1007/s11440-020-01004-9

RESEARCH PAPER

Three-dimensional Wadell roundness for particle angularity characterization of granular soils

Junxing Zheng[1] · **Hantao He**[2] · **Hossein Alimohammadi**[3]

Received: 3 December 2019 / Accepted: 8 June 2020

Abstract
The geologist Hakon Wadell proposed the roundness definition in the 1930s for quantifying the particle angularity of granular soils. Due to the difficulty in obtaining three-dimensional (3D) particle geometries in the 1930s, Wadell used two-dimensional (2D) projections of particles to develop his roundness definition, although it is limited for analyzing 3D particles. This study shows that Wadell's 2D roundness could be extended to a 3D definition. The 3D roundness is defined as the ratio of the average radius of spheres fitting to corners and ridges of a 3D particle to the radius of the maximum inscribed sphere of the 3D particle. A computational geometry algorithm is proposed to automatically identify corners and ridges, fit appropriate spheres to corners and ridges, identify the maximum inscribed sphere of the 3D particle, and compute 3D roundness. The number of slices per diameter of the maximum inscribed sphere of the particle, *NSD*, is defined for controlling the sphere fitting process. The minimum required $NSD = 300$ is established to ensure the reliable use of the proposed 3D computational geometry algorithm. Finally, a total of 20,000 particles from five sand specimens with various angularities are scanned by X-ray computed tomography. The 2D and 3D roundnesses of these 20,000 particles are compared. The 2D roundnesses capture the general trend of the corresponding 3D roundnesses, but vary in a large range, resulting in significant uncertainties when using 2D images to infer 3D particle angularities.

Keywords Computational geometry · Particle angularity · Particle shape characterization · Wadell roundness

1 Introduction

Particle angularity is a fundamental property of granular soils governing the capability of particles for forming interparticle locking. Angular particles have many sharp protrusions (or corners), which can interlock with each other to form a large coordination number and a stronger load-bearing skeleton of granular soils. Experimental and numerical studies have shown that angular soils exhibit larger values of index void ratios, angle of internal friction, dilatancy, constant volume friction angle, compressibility, and small-strain modulus than rounded soils [3, 4, 11, 14, 31, 32, 42, 49, 55, 65, 74, 82, 85, 87, 89]. Recently, more studies have demonstrated the effects of particle shape on other physical behavior of granular soils such as liquefaction and shear banding [38, 75], thermal conductivity and shear wave velocity [39], and soil structural interface [90].

The discrete element method (DEM) has become the preeminent numerical tool for investigating granular

✉ Junxing Zheng
junxing@iastate.edu

Hantao He
hhe@iastate.edu

Hossein Alimohammadi
hosseina@iastate.edu

[1] Department of Civil, Construction and Environmental Engineering, Iowa State University, 354 Town Engineering Building, Ames, MI 50011, USA

[2] Department of Civil, Construction and Environmental Engineering, Iowa State University, 493 Town Engineering Building, Ames, IA 50011, USA

[3] Department of Civil, Construction and Environmental Engineering, Iowa State University, 220 Town Engineering Building, Ames, IA 50011, USA

material behavior. Typical DEM models use circular or spherical particles, but such oversimplified particulate models cannot provide adequately accurate insight into the mechanical behavior of granular soils. Methods to better simulate irregular particle shapes for use in DEM have therefore been sought [83]. Researchers have explored the use of ideal particle shapes, such as ellipsoids, spherical cylinders, pentagons, and rounded-cap elongated rectangles, in DEM simulations [8–10, 16, 18, 28, 41, 52, 76]. These works led to significant progress in the simulation of idealized particle shapes. However, these techniques cannot simulate realistic soil particles with irregular particle shapes. Very recently, various techniques have been developed for simulating realistic particle geometries such as poly-superellipsoid-based approach [79], polyhedral particles [21], and physics engine-based approach [27].

The importance of particle angularity has been recognized in other disciplines dealing with granular materials, such as pavement engineering [43, 50, 62, 63], cement and concrete [24], geology [46], material science [66], mining [29], powder technology [19], chemical engineering [15], pharmaceuticals [20], and agriculture [47].

The angularities of granular soils are quantified by a factor called roundness, which was proposed by the geologist Hakon Wadell in the 1930s [67–69]. Using two-dimensional projections of particles as shown in Fig. 1a, Wadell defined roundness as the ratio of the average radius of curvature of the corners of a particle to the radius of the maximum inscribed circle:

$$R_2 = \frac{\text{average radius of curvature of corners}}{\text{radius of the largest inscribed circle}} = \frac{\sum_{i=1}^{N} r_{2,i}/N}{r_{2,\mathrm{in}}} \quad (1)$$

where $r_{2,\mathrm{i}}$ is the radius of the ith corner circle, N is the total number of corners, and $r_{2,\mathrm{in}}$ is the radius of the maximum inscribed circle, and the subscript “2” means Wadell’s roundness is based on two-dimensional (2D) particle projection.

The original procedure for determining Wadell’s roundness requires considerable manual effort. Each corner on a particle’s outline is compared to a series of transparent templates to find the maximum sized circle that will fit inside the corner. In the 1950s, charts consisting of a set of reference particle silhouettes were prepared to facilitate rapid estimation of Wadell’s roundness through visual comparisons to particles viewed under a microscope. Three such charts were developed by Krumbein [34], Krumbein and Sloss [35], and Powers [53]. The manual method is tedious, and the chart method is subjective. Both methods are difficult to implement on a large number of particles [30].

Advances in optical image gathering have led to the rapid digitization of soil particle projections and created a potential to automate Wadell’s procedure. However, automation is a considerably challenging mathematical problem, and thus, researchers have proposed alternative definitions of roundness, which could be more easily computerized. Such alternative definitions have included: Fourier analysis [13, 71, 73], angularity index [2, 58], and a fractal technique [7, 23]. A comprehensive review of these newer methods was provided by Masad et al. [44]. However, the alternative definitions of roundness have not yet prevailed over Wadell’s, owing to the latter’s longer history, a large body of research based on it, and numerous useful correlations to mechanical properties based on it.

In light of its continuing popularity and wide usage, Zheng and Hryciw [81, 84] developed a computational geometry algorithm to automate Wadell’s roundness. This code can automatically read binary particle projections (Fig. 1a–c), identify corners, fit appropriate circles to corners, compute the maximum inscribed circles to the particles, and compute R_2 values based on Eq. (1). This technique eliminates the subjectivity in roundness computation. To facilitate researchers to use the computational

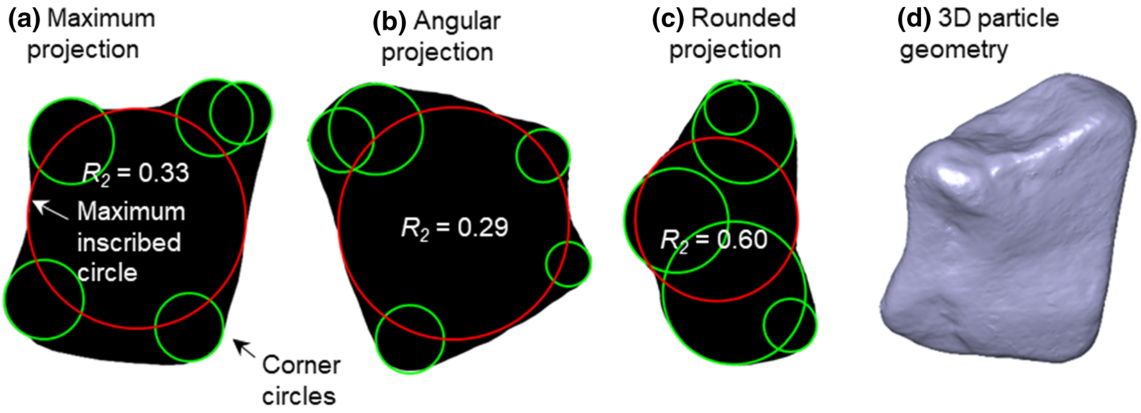

Fig. 1 Definition of R_2 and the shortcomings of R_2 for characterizing the angularity of 3D particle

geometry code, the source code has been posted online so that researchers are free to download, extend, and customize the code based on their needs. To date, this code has been frequently used by researchers in various disciplines; some of their publications include [1, 12, 17, 22, 25, 26, 40, 45, 51, 54, 56, 57, 64, 65, 70, 72, 78].

In fact, three projections in Fig. 1a–c are from the same three-dimensional (3D) soil particle shown in Fig. 1d, but they appear completely different as three different particles. The computed R_2 values vary in a wide range from 0.29 to 0.60. Essentially, each view direction of the 3D soil particle (except for sphere) will yield an entirely new 2D image and a new R_2. Wadell suggested using the maximum projections of particles for R_2 computation, merely because of the ease in obtaining the maximum projections, not because of the correctness. When spreading particles on a flat surface, the particles will naturally show the maximum projection upward under gravity. Therefore, it is easy to trace the particle perimeter for roundness analysis.

Uncertainties in R_2 definition for characterizing angularities of 3D particles limit the usage of this fundamental soil property. Therefore, although it has been well established that particle angularity affected macro mechanical behavior of granular soils, this fundamental property was commonly ignored by engineers in their practice and not used in classification (e.g., Unified Soil Classification System) of coarse-grained soils due to the inherent limitations of 2D definitions for characterizing 3D particle shapes.

Today, geotechnical engineers have utilized various 3D imaging techniques for capturing 3D particle geometries, such as X-ray computed tomography (X-ray CT) [5, 33, 48, 59, 60], laser scanning technique [6, 37, 77], stereophotography [80, 86, 88], and structured light technique [61]. Therefore, obtaining 3D particle geometries does not remain an obstacle for quantifying 3D particle angularity. 3D computer vision techniques for analyzing 3D particle geometries have been developed. For example, Lai and Chen [36] reconstructed granular particles from X-ray CT using the machine learning and level set method. However, the computer vision techniques for determining 3D Wadell roundness are absent. The paper aims to extend Wadell's 2D roundness definition to develop a 3D roundness definition. Then, 3D computational geometry techniques are developed to analyze particle geometries to determine the 3D roundness automatically.

2 Development of 3D roundness definition

The geometric structure of a 3D soil particle surface includes corners, flat parts, concave parts, and ridges. The corners and ridges are protrusions on the particle surface, as shown in Fig. 2. The protrusions of particles interact with each other creating interparticle locking and forming the soil skeleton. The ridges are important features on the particle surface, while the corners are essentially intersections of several ridges. However, the ridges are either occluded or projected as corners in the 2D particle projection. Wadell's 2D roundness definition can be naturally extended to 3D by evaluating the sharpness of corners and ridges of particles. Therefore, the 3D roundness (R_3) can be defined as:

$$R_3 = \frac{\text{average radius of corner and ridge spheres}}{\text{radius of the largest inscribed sphere}} = \frac{\sum_{i=1}^{N} r_{3,i}/N}{r_{3,\text{in}}} \tag{2}$$

where $r_{3,\text{i}}$ is the radius of the kth corner or ridge sphere, N is the number of detected corner and ridge spheres, and $r_{3,\text{in}}$ is the radius of the maximum inscribed sphere, and the subscript "3" means newly proposed roundness definition is based on 3D particle geometry. Computation of R_3 requires determining the maximum inscribed sphere, identifying corners and ridges, and fitting appropriate spheres to corners and ridges of 3D particles. A computational geometry algorithm is developed in this study to determine these parameters.

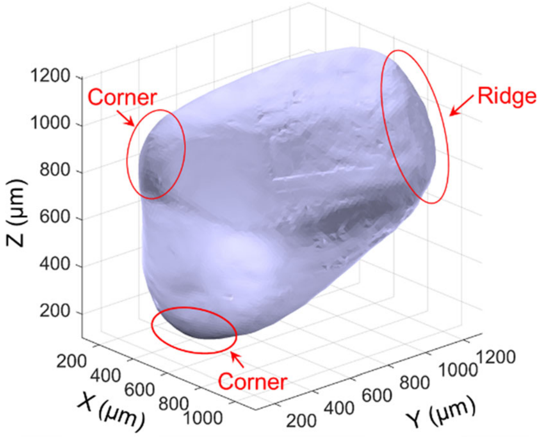

Fig. 2 Protrusion parts on 3D soil particle

3 Determination of the maximum inscribed sphere

Zheng and Hryciw [81] showed that the maximum inscribed circle of a 2D particle projection can be determined using a 2D Euclidean distance map. The same concept is used to determine the maximum inscribed sphere of a 3D particle. A 3D Euclidean distance map of a 3D particle geometry is computed by determining the distance of each point inside the particle to the nearest boundary as shown in Fig. 3a. The point O located at (572, 608, 720) having the maximum distance value identifies the center of maximum inscribed sphere $S_{\max}$. The distance value at point O, which is 390 µm, is the radius of the maximum inscribed sphere $r_{3,\mathrm{in}}$. The determined maximum inscribed sphere is superimposed to the original particle in Fig. 3b.

3.1 3D computational geometry to determine R_3

The identification of corners on 3D particles is challenging because of the highly irregular nature of soil particles. Significant variances exist in the numbers and curvatures of corners on the same particle and certainly the corners on many particles. The 3D particles are more complicated than the 2D projections due to new features, ridges, which is either occluded or projected as corners in 2D particle projections. It is difficult to establish a rigorous and repeatable procedure for a computer to follow. Another issue is that surface roughness is superimposed on the soil particle surface. Humans can intuitively distinguish the roughness from small and sharp corners while computer must be taught to do so. This paper developed a 3D computational geometry algorithm to solve these issues.

Figure 4 illustrates the basic concept of the 3D computational geometry algorithm using the example particle in Figs. 2 and 3. We assumed that an appropriate corner sphere S_1 has been fitted to corner 1. The S_1 is located at (330, 484, 268) with a diameter of 167 µm. Then, we use slices in X, Y, and Z directions to cut through the corner 1 and S_1 as shown in Fig. 4a, c, and e. Figure 4b, d and f shows the intersections of these slices with soil particle geometry and S_1. In these slices, the cross sections of corner sphere S_1 become circles having the same center but different radii, which are fitting corners of particle boundary. This observation establishes the linkage between 3D corner spheres and 2D corner circles. Therefore, if we discrete particles into slices and identify corner circles in all the slices, concentric circles (circles located at the same center) in the consecutive slices may belong to a corner sphere, which can be used to identify and reconstruct corner spheres.

Based on the analysis above, the following algorithm is designed in Fig. 5 to identify corner and ridge spheres. The overall algorithm contains three basic steps. Firstly, the 3D particle geometry is discretized into slices. Then, each slice is input into the 2D roundness computational algorithm developed by Zheng and Hryciw [81].

Zheng and Hryciw's [81] algorithm removes the surface roughness superimposed on the perimeter and determines a mean surface using two statistical techniques, including locally weighted scatter plot smoothing (LOESS) and K-fold cross-validation. Then, a loop algorithm is developed to identify the corners and fit appropriate circles to corners.

In the last step, all the computed circles from different slices are analyzed. The concentric circles in the consecutive slices are used to reconstruct the corner and ridge spheres.

3.2 Discretize particle into slices and identify corner circle in slices

The particle is discretized into slices in three directions along X, Y, and Z axes such as Fig. 4a, c, and e. In fact, the number of slicing directions required for identifying

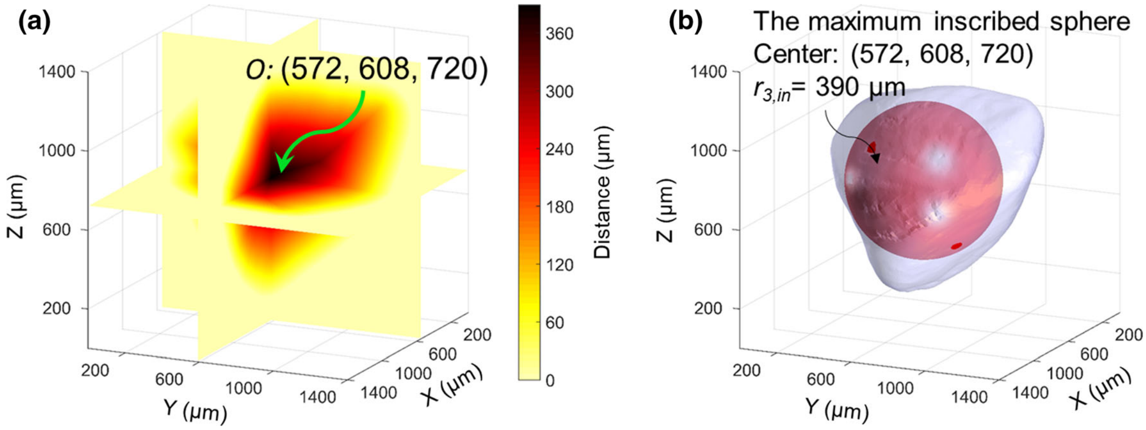

Fig. 3 Determination of the maximum inscribed sphere

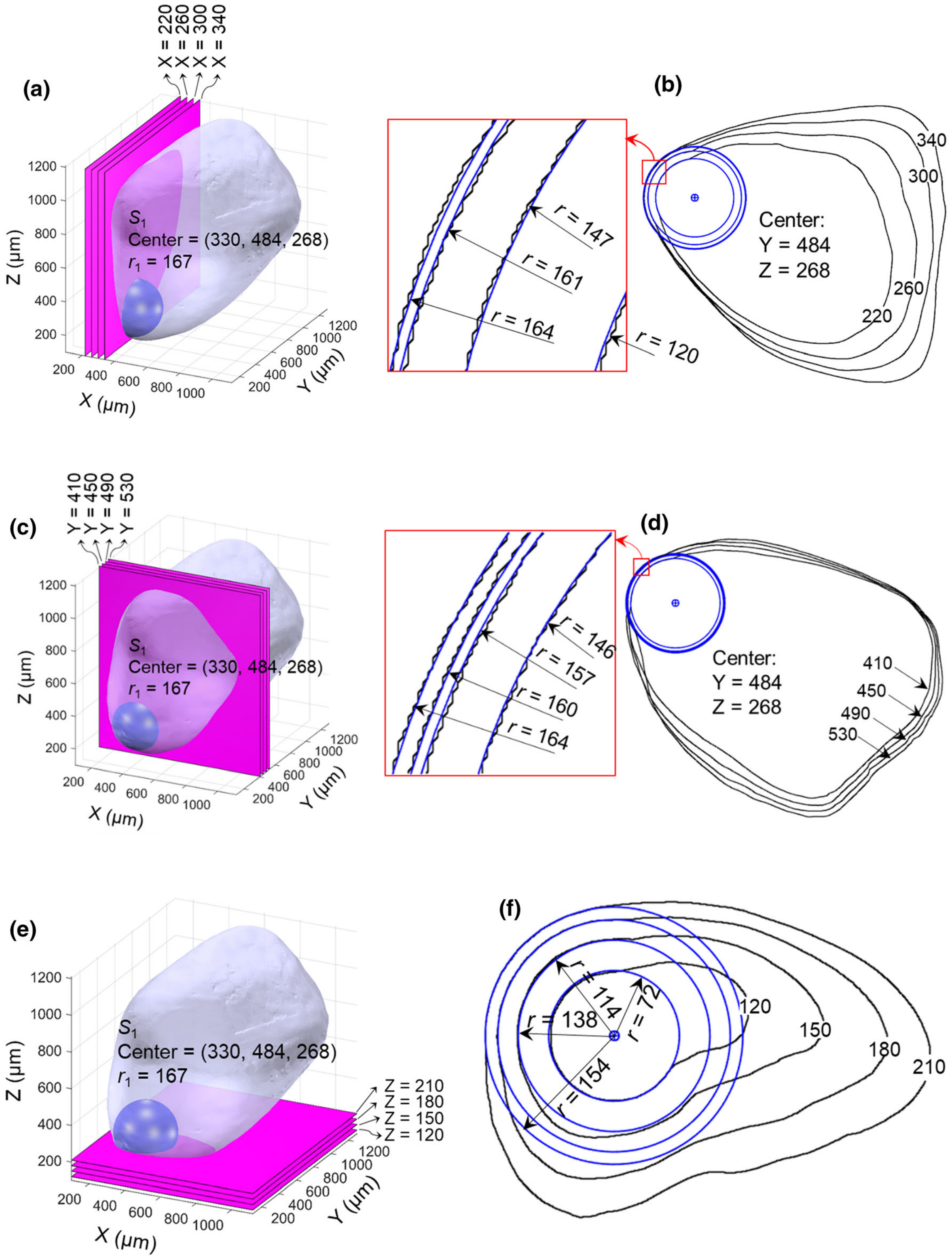

Fig. 4 Relationship between 2D corner circles and 3D corner spheres (unit is in μm)

corners and ridges on particles depends on particle angularity: Rounded particles require fewer slicing directions while angular particles require more. The extreme case is a sphere that requires one slicing direction. However, using slices in one direction may not be adequate to find all the corner and ridge spheres for angular particles. As will be shown in Fig. 12, there are 31, 38, and 26 corner spheres found using slices in *X*, *Y*, and *Z* directions. Some corners

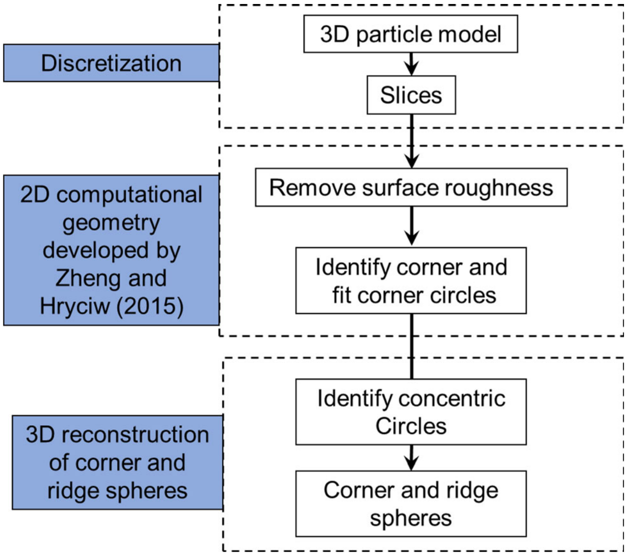

Fig. 5 Overview of the 3D computational geometry algorithm

and ridges are not identified using slices in one direction, because the soil particle appears different in different view angles: Some corners are visible in one direction but not in the other direction. Therefore, multiple slicing directions are necessary for analyzing angular particles.

In this study, a total of 8000 angular particles were selected from crushed limestone (Fig. 16a) and crushed Gabbro (Fig. 16b). These 8000 particles are analyzed to determine the minimum number of slicing directions. We find that using three slicing directions along with X, Y, and Z axes ensures all the corners and ridge spheres can be identified for these 8000 angular particles. Three slicing directions adequate will naturally satisfies less angular particles. Therefore, this study suggests that using three slicing directions along with X, Y, and Z axes for discretizing particles generates, and this criterion generates satisfactory results for most particles encountered in practice. If readers have specialized soils requiring more slicing direction, they can rotate the particles by an angle and using three slicing directions along with X, Y, and Z axes to discretize the particle again to generate more slicing directions to analyze particle angularity.

The slicing interval Δ controls the number of slices and, therefore, is key to the reliability and accuracy of the proposed 3D computational geometry algorithm. However, the Δ depends on particle sizes. Naturally, small particles require small Δ. Therefore, to eliminate the effects of particle size, a dimensionless parameter *NSD* (the number of slices per diameter of the maximum inscribed sphere of the particle) is defined. The diameter of the maximum inscribed sphere of a particle is related to the particle size. Therefore, by establishing the minimum required *NSD* value, the Δ can be back-calculated. The minimum required *NSD* value that ensures reliable roundness calculations will be investigated in Sect. 5 of this paper. At this point, we will use $NCD = 156$ for the demonstration of the developed methodologies. The diameter of the maximum inscribed sphere of the example particle in Fig. 3 is 780 µm. Therefore, the interval between slices Δ is 5 µm. The particle is discretized with an interval of 5 µm in X, Y, and Z directions, generating a total of 669 slices, including 205 slices in the X direction, 241 slices in the Y direction, and 223 slices in the Z direction.

Each slice is input into the 2D computational geometry algorithm to compute appropriate corner circles. The results for seven slices in the Z direction are shown in Fig. 6. Three circles (C_1, C_2, and C_3) are fitted into three corners on each slice.

3.3 Reconstruction of corner and ridges spheres from concentric circles

After finding corner circles for each slice, the next step is to search concentric corner circles. However, due to the angular nature of soil particles and the computational round-off, the computed centers of corner circles rarely have the same coordinates. For example, the circles C_1 of slices $Z = 155$ to 185 in Fig. 6 belong to a corner sphere. Centers of C_1 at different slices are very close but not identical. We found that the divergence of coordinates of centers of concentric circles is typically within $0.013 \times r_{3,\text{in}}$, where $r_{3,\text{in}}$ is the radius of the maximum inscribed sphere. In this example, $\Delta = 5$ µm.

A total of 53 corner circles are founded in the slices $Z = 120$ to 210 (19 slices in the Z direction and seven slices are shown in Fig. 6). The coordinates of centers of these 53 corner circles are plotted in Fig. 7a. A square window having a size of $\Delta \times \Delta$ (e.g., 5×5 µm in this example) is used to scan through all the centers as shown in Fig. 7a. Two scanning squares containing more than one center are founded: square 1 contains 19 centers, and square 2 contains 3 centers. Square 1 is magnified in Fig. 7b. The 19 circles included in square 1 are used to reconstruct a corner sphere.

These 19 concentric circles in square 1 are plotted in the 3D particle geometry in Fig. 8. Figure 8a and c is the oblique view and front view of the same corner, which are enlarged in Fig. 8b and d. These concentric circles depict the shape of a corner sphere. The next step is to reconstruct the corner sphere using these concentric circles.

The X and Y coordinates of centers of the corner sphere can be determined as the average of the X and Y coordinates of centers of these 19 circles, which are $X = 326$ and $Y = 483$ as shown in Figs. 7b and 8. The Z coordinate and the radius of the corner sphere are unknown and assumed as Z_s and r_s, respectively, as shown in Fig. 8b and d. If we

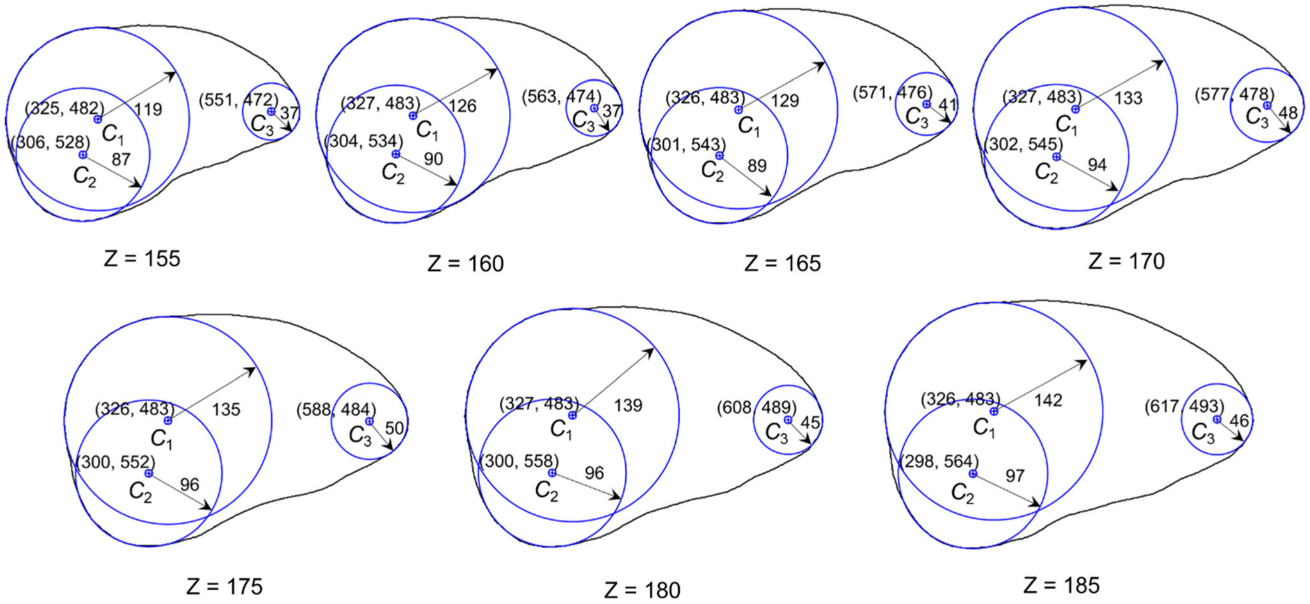

Fig. 6 2D corner circle for seven slices in the Z direction (the unit is in μm)

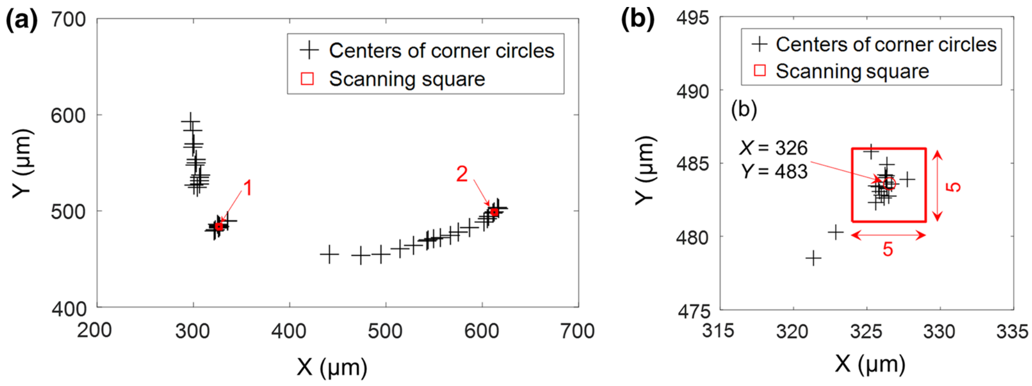

Fig. 7 Identification of concentric circles

connect the center of corner sphere O_s, the center of the ith concentric circle O_i, and a point C on the ith concentric circle, a triangle $\Delta O_s O_i C$ is constructed as shown in Fig. 8b and d. Therefore, the following relationship can be found:

$$(Z_s - Z_i)^2 + r_i^2 = r_s^2 \tag{3}$$

where Z_i and r_i are the Z coordinate and radius of the ith concentric circle.

In Eq. (3), there are two unknowns of Z_s and r_s. Once we determine Z_s and r_s, the best-fitting sphere to this corner can be uniquely determined. At least two concentric circles are required to solve Eq. (3). Usually, there will be more than two concentric circles are found at the same location. A system of nonlinear equations will be generated. A least square method is used to search the optimized Z_s and r_s. The results for the above example are $Z_s = 268$ and $r_s = 167$. The computed corner sphere is shown in Fig. 9, which is well fitted to the corner. The above process illustrates the process of fitting one corner sphere.

Generally, the corner circles centered in the scanning square of $\Delta \times \Delta$ do not necessarily belong to a unique corner sphere. Therefore, a more general algorithm is presented herein. For example, Fig. 10a shows a part of particle surface in the Y–Z plane trimmed from a soil particle. It has a complicated surface structure with three consecutive corners. In Fig. 10b, 41 slices cut through the surface along the Z axis. The 2D computational geometry algorithm is used to compute the corner circles at each slice as shown in Fig. 10c. A total of 35 concentric circles are found. The X and Y coordinates of all these 35 concentric circles are all in the same $\Delta \times \Delta$ square with an average center of (X_0, Y_0). For the ith concentric circle, the Z coordinate and radius are Z_i and r_i, respectively. The process of reconstructing those concentric circles into three corner spheres is the following.

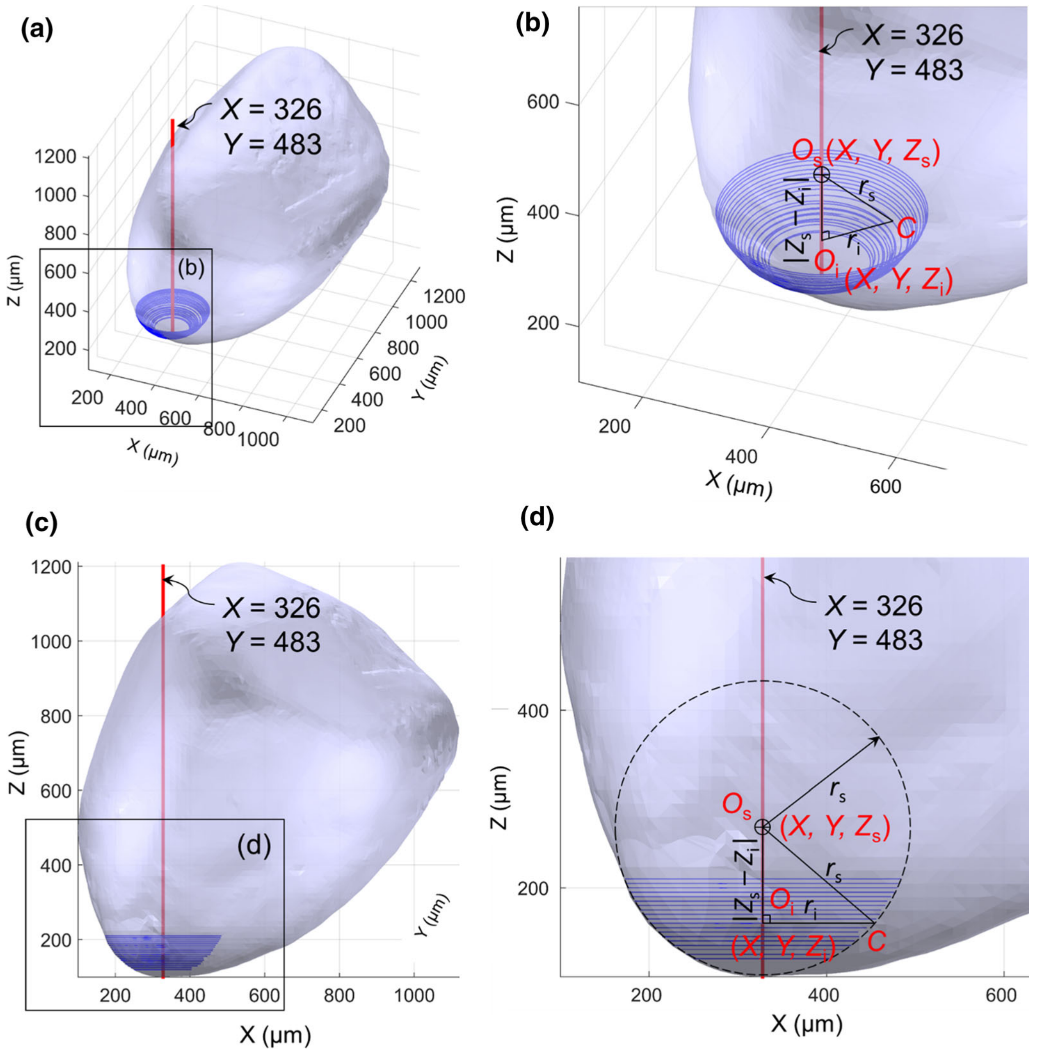

Fig. 8 Fitting process for the corner sphere

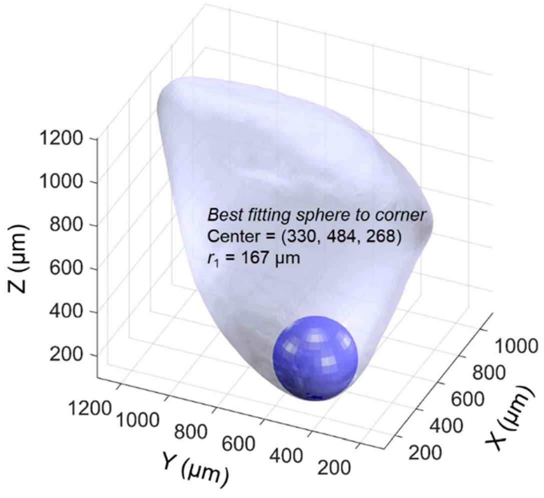

Fig. 9 Reconstruction of corner spheres from the 19 concentric circles

Firstly, all the #1 to #35 concentric circles are used to find a best-fitting sphere using Eq. (3), resulting in a sphere located at (X_0, Y_0, Z_s) with a radius of r_s as shown in Fig. 10d. The minimum distance from the center (X_0, Y_0, Z_s) to the 3D particle surface is $d_{\min}$. If $d_{\min}$ is smaller than r_s, the best-fitting corner sphere extrudes particle surface, which is not satisfactory. Then the #35 circle is eliminated from fitting. The last circle moves to the #34 circle.

The #1 to #34 circles are now used to fit a new sphere. The recomputed $d_{\min}$ and r_s are compared again. The $d_{\min}$ is still smaller than r_s. Then #34 circle is eliminated, and the #33 circle becomes the last one. Such process will continue until finding a sphere satisfying $r_s = d_{\min}$ or there is only one circle remaining for fitting. Figure 10e shows the last corner circle moves to the #29 circle, but no satisfactory sphere is found. When the last corner circle moves to the #13 circle in Fig. 10f, the first corner sphere satisfying $r_s = d_{\min}$ is found. The #1 to #13 circles are fitted

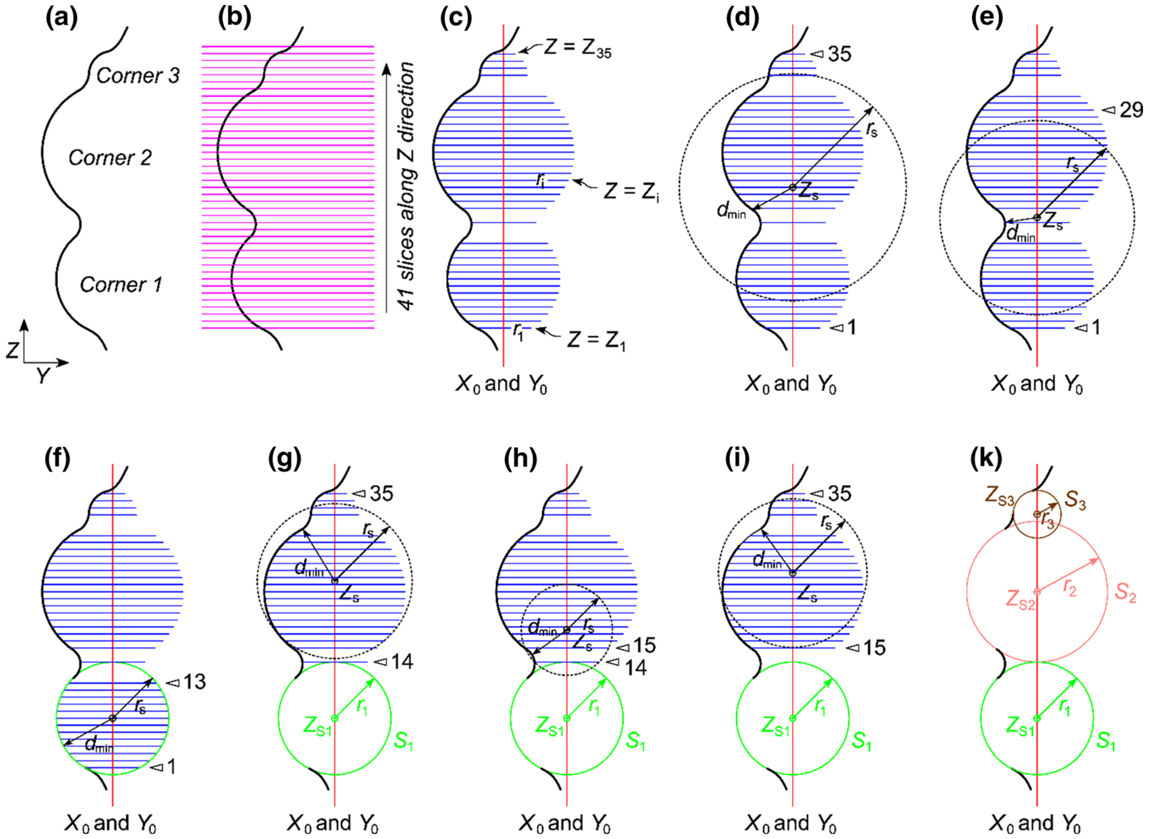

Fig. 10 General algorithm of reconstructing corner spheres from concentric circles

to the first corner sphere, and they are permanently removed from the fitting process.

In the next step, the first circle moves to the #14 circle, and the last circle moves back to the #35 circle. The #14 to #35 circles are used to fit a sphere in Fig. 10g. The r_s and d_{min} are recomputed and compared again. The above process is repeated. However, when the last circle moves back to the #15 circle, there is still no satisfying sphere as shown in Fig. 10h. Then the #14 circle is permanently removed without finding a corner sphere.

The first circle moves to the #15 circle, the last circle moves back to the #35 circle as shown in Fig. 10i, and the above process continues. The final fitting results are shown in Fig. 10k. As expected, three corner spheres are fitted to three corners.

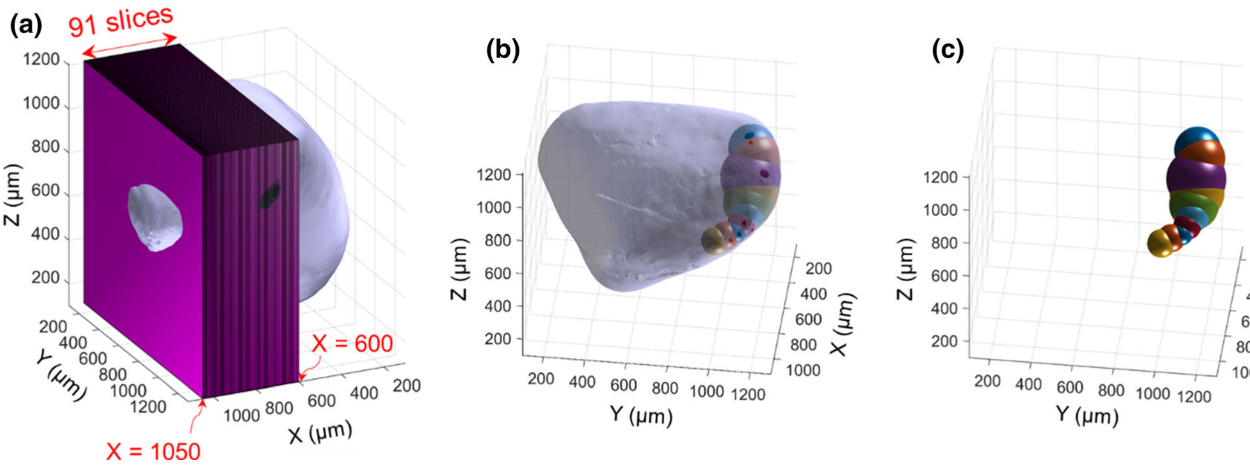

Fig. 11 Reconstruction of ridge spheres

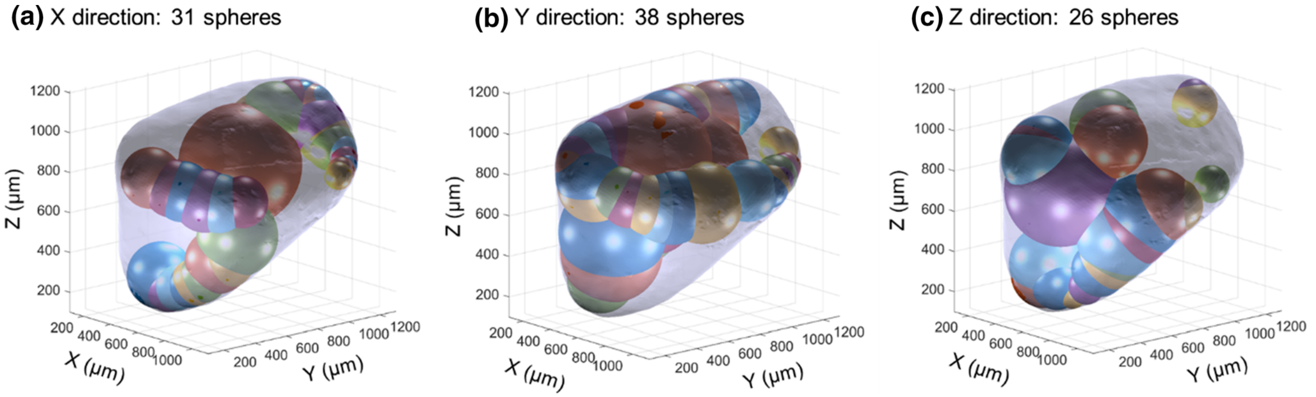

Fig. 12 Best-fitting spheres using slices in X, Y, and Z directions, respectively

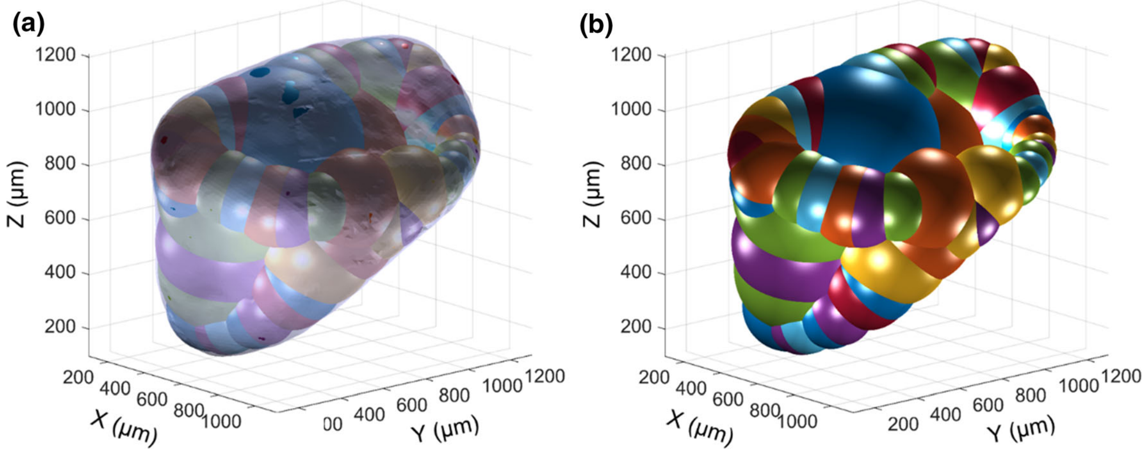

Fig. 13 Final corner and ridge spheres by combining best-fitting spheres in three directions

The above algorithm can be extended to find the best-fitting spheres to ridges. An example is shown in Fig. 11. A total of 91 slices cut through a ridge on the 3D particle as shown in Fig. 11a. Using the algorithm described above, ten spheres are reconstructed, which are well fit the ridge. Figure 11b superimposes these ten spheres on the soil particle surface, while Fig. 11c only shows these ten spheres.

The above algorithm is used to reconstruct corner and ridge spheres from all the slices in the X, Y, and Z directions. There are 31, 38, and 26 corner spheres are found using slices in X, Y, and Z directions as shown in Fig. 12a–c, respectively. The computed spheres are not the same in different directions because the soil particle appears different in different view angles: Some corners are visible in one direction but not in the other direction.

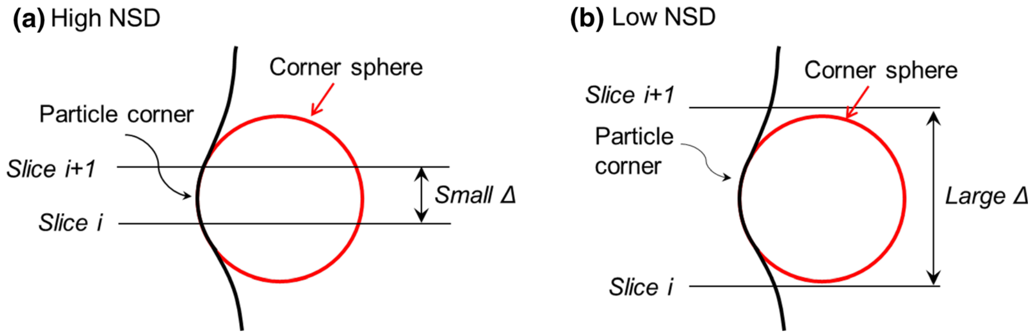

Fig. 14 Physical meaning of *NSD* and Δ

(a) Angular particle

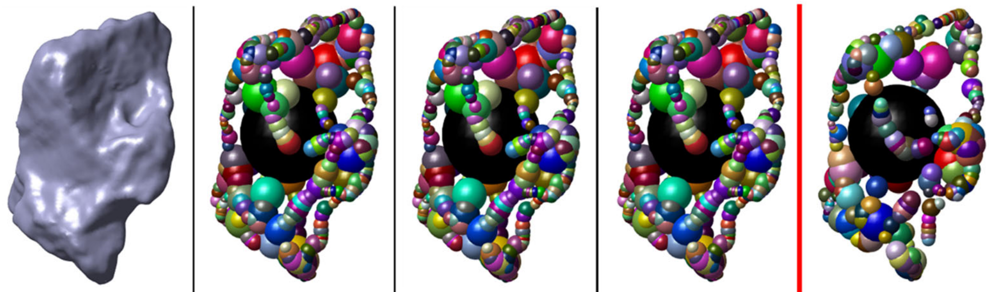

NSD	1200	700	300	200
N	379	379	378	266
R_3	0.17	0.17	0.17	0.21

(b) Sub-angular particle

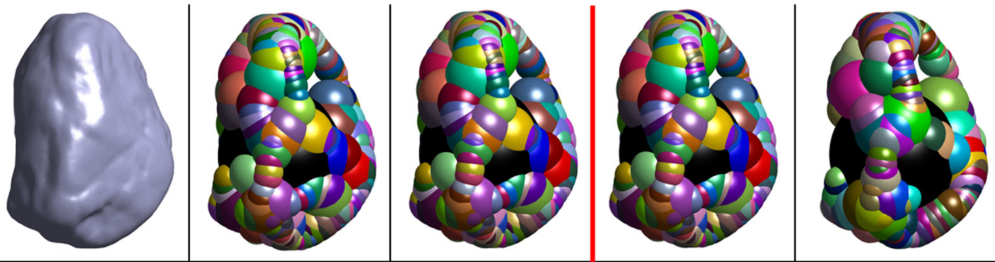

NSD	700	300	200	100
N	179	179	178	142
R_3	0.35	0.35	0.35	0.39

(c) Sub-rounded particle

NSD	300	200	100	50
N	179	179	178	142
R_3	0.35	0.35	0.35	0.39

(d) Rounded particle

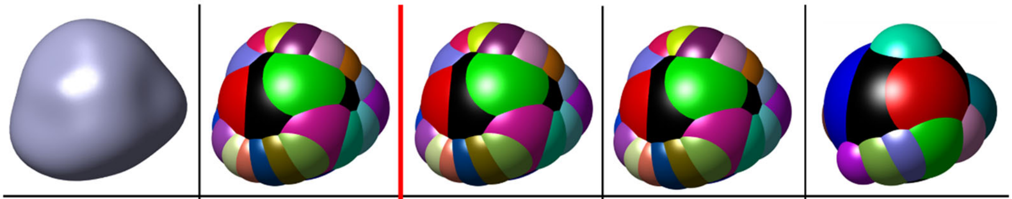

NSD	300	200	100	50
N	28	28	28	21
R_3	0.70	0.70	0.70	0.78

Fig. 15 Effects of *NSD*s on the 3D roundness computational results (the black spheres are the maximum inscribed sphere and corner and ridges spheres are in other colors)

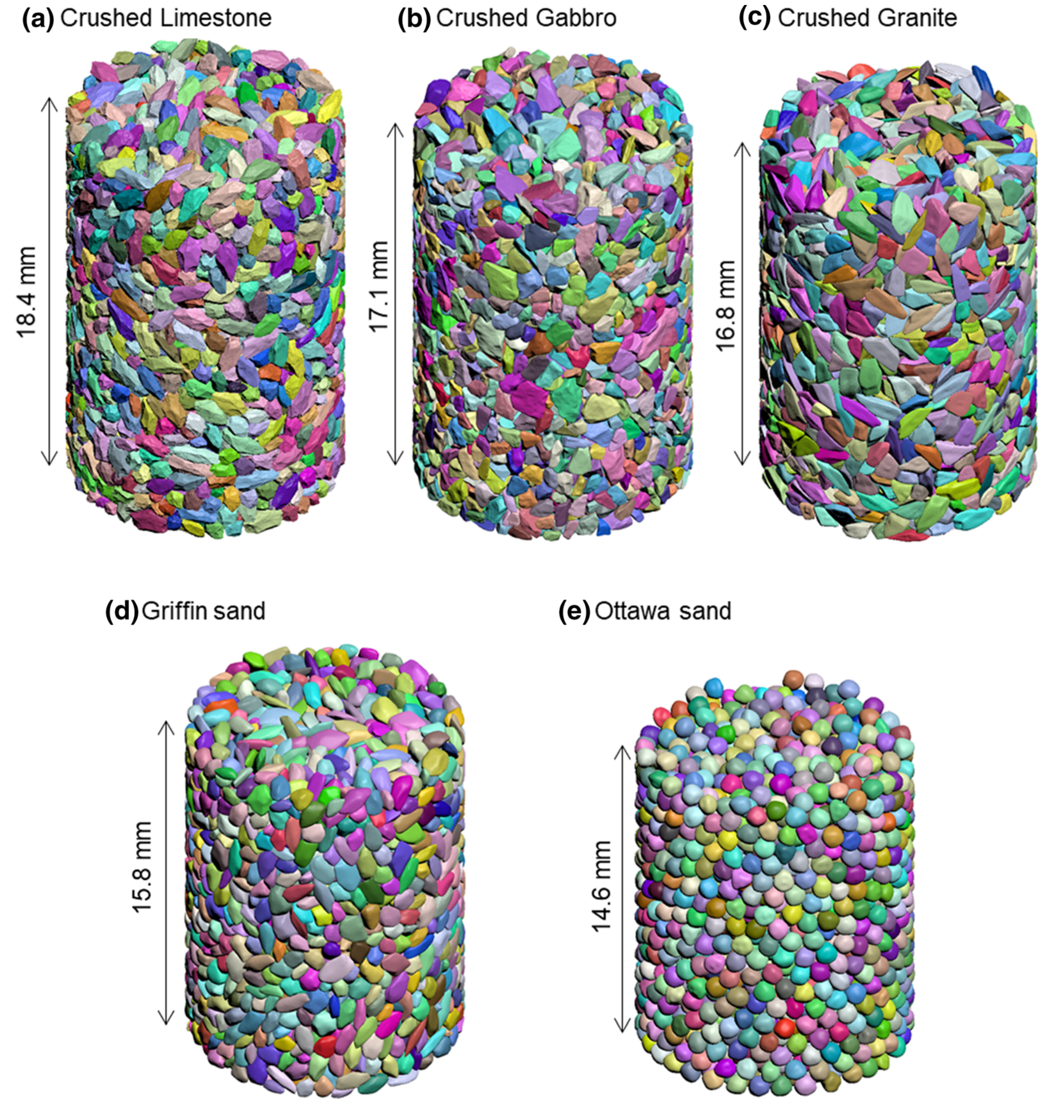

Fig. 16 Five sand specimens scanned by X-ray computed tomography (X-ray CT)

The next step is to combine all the corner spheres from three directions. The common corner spheres obtained from three directions are merged into one sphere. Then, a total of 54 spheres are determined. Figure 13a superimposes these best-fitting corner and ridge spheres into soil particle surface, and Fig. 13b shows the best-fitting spheres. The average radius of the corner and ridge spheres is 236 µm. According to Eq. 3, 3D roundness is computed as $R_{3D} = 236/390 = 0.61$.

4 Analysis of *NSD*

The physical meaning of *NSD* (number of slices per diameter of the maximum inscribed sphere of particle) is shown in Fig. 14, which essentially sets a threshold between corner and non-corner on soil particle surface. A large *NSD* generates a small slicing interval Δ as shown in Fig. 14a, while low *NSD* generates a large slicing interval Δ as shown in Fig. 14b. Therefore, assuming the corner in Fig. 14 is the smallest corner on a soil particle, the *NSD* must be sufficiently large so that at least two slices cut through this corner. Then, a corner sphere can be reconstructed by two concentric circles. Once the smallest corner is identified, further increasing *NSD* does not change the results, but generates more slices and dramatically increases computational loads.

The *NSD* depends on particle angularity. For a rounded particle consisting of large corners, a small *NSD* value is enough to identify all the corners. Nevertheless, for an angular particle, a large *NSD* is necessary to detect its small and sharp corners. Therefore, an angular particle is investigated as the worst-case scenario to determine minimum *NSD* value ($NSD_{\min}$) as shown in Fig. 15a. A series of *NSD*

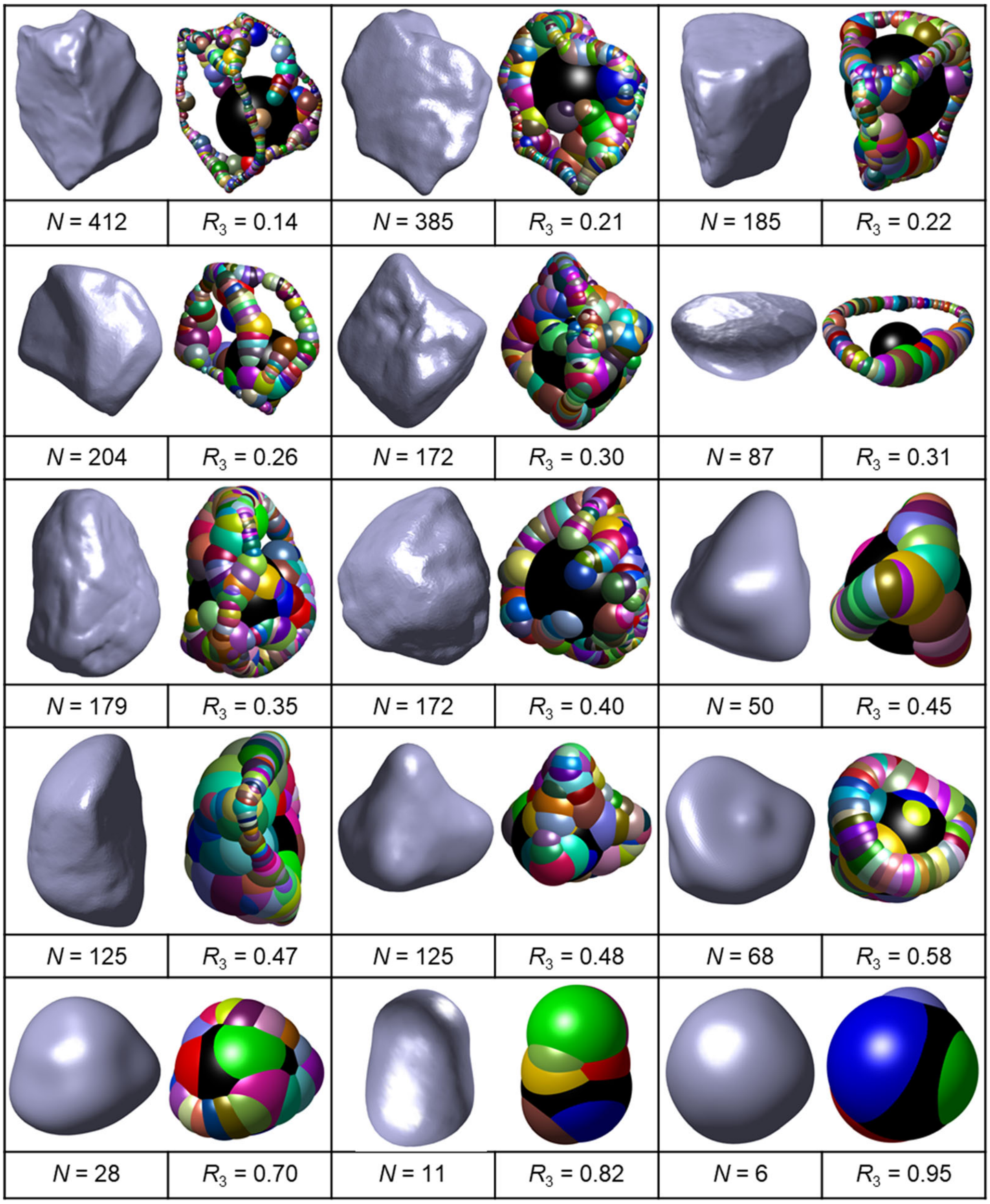

Fig. 17 3D roundness computational results of 15 particles randomly selected from 20,000 particles of five sands (the black spheres are the maximum inscribed sphere, and corner and ridges spheres are in other colors)

values are used in 3D computational geometry algorithm to determine R_3 values as shown in Fig. 15a. When *NSD* decreases from 1200 to 300, the number of identified corner and ridge sphere N and determined R_3 keep constant. Therefore, the $NSD_{\min} = 300$ gives reliable results for this angular particle, which is selected as a criterion for using the proposed 3D computational geometry.

This trial and error process is repeated for the other three particles with subangular to rounded shapes as shown in Fig. 15b–d. A series of *NSD* values are used to determine R_3 values. As shown, more rounded particles require smaller $NSD_{\min}$ values. However, the $NSD_{\min} = 300$ adequate for the angular particle in Fig. 15a satisfies less angular particles in Fig. 15b–d. Therefore, the criterion of $NSD_{\min} = 300$ is defined for using 3D computational geometry algorithm.

5 Comparison between 2D and 3D roundnesses

Five sand specimens were used in this study to evaluate and effectiveness of the proposed 3D roundness definition, 3D computational geometry algorithm, and compare 2D

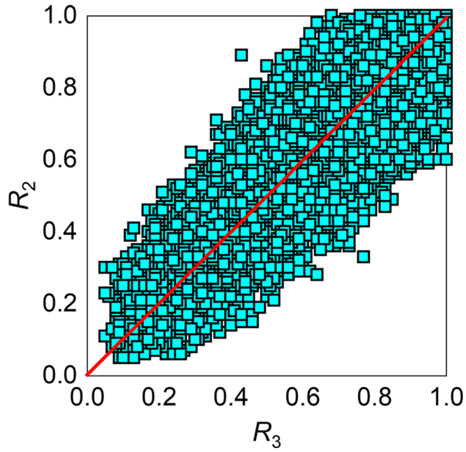

Fig. 18 Comparison between R_2 and R_3 values of 20,000 particles from five sands

and 3D roundnesses. They included crushed limestone (very angular to angular particles), crushed Gabbro (very angular to subangular particles), crushed granite (very angular to subangular particles), Griffin sand (subangular to subrounded particles), and Ottawa sand (rounded to well-rounded particles). For each sand, we manually picked 4000 particles in a range of #30 sieve (0.595 mm) to #18 sieve (1.00 mm). These five sand specimens may be representative of commonly used sands in geotechnical research and practice.

For each soil, these 4000 particles were spread on a flat surface, and an image was captured above, which generated the maximum projections of particles. The 2D computational geometry code was used to determine R_2 values.

Then, for each sand, selected particles were funneled into a 12-mm-diameter plastic cylinder and were vibrated to generate a dense specimen. A high-resolution X-ray computed tomography (X-ray CT) was used to scan specimens with a resolution of 10 µm/voxel, which yielded 3D volumetric images. An improved watershed analysis technique proposed by Sun et al. [60] was used to process volumetric images, segment contact particles, and identify individual particles. A total of 4000 particles were determined for each sand specimen, which verified the reliability of particle segmentation results. These particles are plotted in different colors in Fig. 16.

The *NSD* = 300 was used in the discretization. The 3D computational geometry code developed by this study was used to determine R_3 values of these 20,000 particles. Fifteen typical particles are randomly selected to illustrate the computational results as shown in Fig. 17. The maximum inscribed spheres are plotted in the black color, while corner and ridge spheres are plotted in other colors. The computed spheres well fit the corners and ridges of all the particles having very angular to well-rounded shapes.

The R_2 and R_3 values of 20,000 particles are compared in Fig. 18. The R_2 values capture the general trend of the R_3 values, but vary in a large range, resulting in significant uncertainties when using 2D images to infer 3D particle shapes. Based on the comparisons, geotechnical engineers should be cautious when using 2D images to characterize 3D particle shapes. As 3D imaging techniques are increasingly available to common soil testing laboratory, the 3D roundness and the associated computational geometry techniques developed by this study allow geotechnical engineers to accurately characterize 3D angularities of granular soils.

6 Discussion

The geometric structure of a 3D soil particle surface includes corners, flat parts, concave parts, and ridges as shown in Fig. 19a. The proposed techniques can successfully identify corners, ridges, saddle-shaped ridges, and fit appropriate spheres as shown in Fig. 19b. In fact, the concave parts interlock with corners and ridges to form soil skeleton, impacting soil mechanical behavior. However, Wadell's roundness only evaluates the sharpness of corners and ridges. The concave parts are not considered in analyzing particle shape. A new roundness definition should be proposed and evaluated by considering concave parts, corners, and ridges in the future.

7 Conclusions

This study extends the Wadell's 2D roundness (R_2) definition to 3D roundness (R_3) definition. A 3D computational geometry algorithm is proposed by extending the previously developed 2D computational geometry algorithm. The 3D computational geometry can automatically determine the maximum inscribed sphere, identify corners and ridges of 3D particles, and fit appropriate spheres to corners and ridges, and compute R_3 values.

A parameter called *NSD* (number of slices per diameter of the maximum inscribed sphere of particle) is proposed as a controlling parameter for the 3D computational geometry algorithm. Higher *NSD* is required for angular particles, while smaller *NSD* is sufficient for rounded particles. Therefore, the minimum *NSD* ($NSD_{\min}$) is determined as 300 based on investigations of a very angular particle. This $NSD_{\min}$ = 300 can naturally be applicable to less angular particles.

Five sands with a spectral of particle angularities were scanned by X-ray CT, yielding a database containing 20,000 particle geometries. These particles were analyzed by 2D and 3D computational geometries technique to

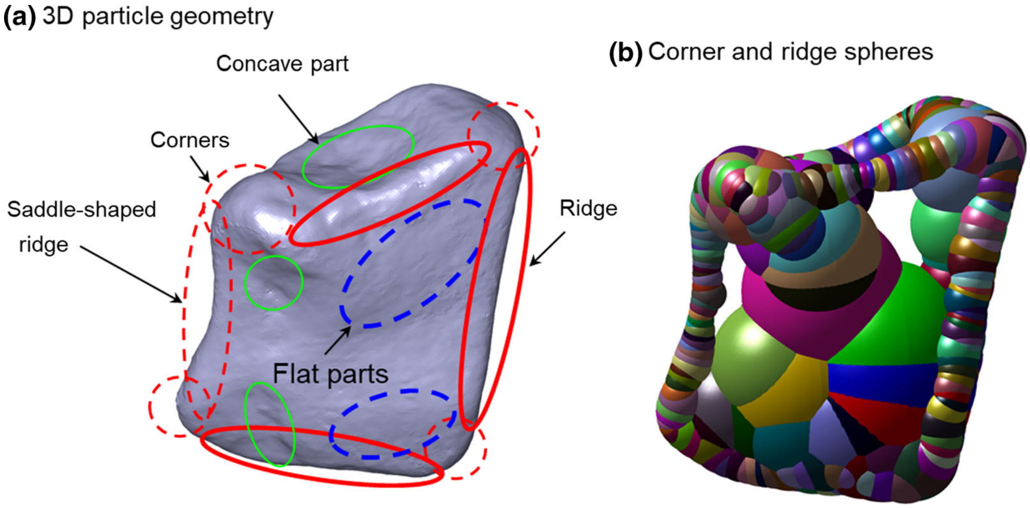

Fig. 19 Concave parts and saddle-shaped ridges

determine R_2 and R_3 values. The R_2 values captured general trends of the corresponding R_3 values, but varied within large ranges, resulting in significant uncertainties when using 2D images to infer 3D particle shapes.

Acknowledgements This material is based upon work supported by the U.S. National Science Foundation under Grant No. CMMI 1917332. Any opinions, findings, and conclusions or recommendations expressed in this material are those of the authors and do not necessarily reflect the views of the National Science Foundation.

References

1. Al-Rkaby AHJ, Chegenizadeh A, Nikraz HR (2017) Anisotropic strength of large scale geogrid-reinforced sand: experimental study. Soils Found 57:557–574. https://doi.org/10.1016/j.sandf.2017.03.008
2. Al-Rousan T, Masad E, Tutumluer E, Pan T (2007) Evaluation of image analysis techniques for quantifying aggregate shape characteristics. Constr Build Mater 21:978–990. https://doi.org/10.1016/j.conbuildmat.2006.03.005
3. Altuhafi FN, O'Sullivan C, Cavarretta I (2013) Analysis of an image-based method to quantify the size and shape of sand particles. J Geotech Geoenviron Eng 139:1290–1307. https://doi.org/10.1061/(asce)gt.1943-5606.0000855
4. Altuhafi FN, Coop MR, Georgiannou VN (2016) Effect of particle shape on the mechanical properties of natural sands. J Geotech Geoenviron Eng 142:1–15. https://doi.org/10.1061/(ASCE)GT.1943-5606.0001569
5. Andrade JE, Lim KWK-W, Avila CF et al (2012) Granular element method for computational particle mechanics. Comput Methods Appl Mech Eng 214–244:262–274. https://doi.org/10.1016/j.cma.2012.06.012
6. Anochie-boateng JK, Komba JJ, Mvelase GM (2013) Three-dimensional laser scanning technique to quantify aggregate and ballast shape properties. Constr Build Mater 43:389–398. https://doi.org/10.1016/j.conbuildmat.2013.02.062
7. Arasan S, Akbulut S, Hasiloglu AS (2011) The relationship between the fractal dimension and shape properties of particles. KSCE J Civ Eng 15:1219–1225. https://doi.org/10.1007/s12205-011-1310-x
8. Azéma E, Radjaï F (2010) Stress–strain behavior and geometrical properties of packings of elongated particles. Phys Rev E. https://doi.org/10.1103/physreve.81.051304
9. Azéma E, Radjaï F, Peyroux R, Saussine G (2007) Force transmission in a packing of pentagonal particles. Phys Rev E. https://doi.org/10.1103/physreve.76.011301
10. Azéma E, Radjai F, Saussine G (2009) Quasistatic rheology, force transmission and fabric properties of a packing of irregular polyhedral particles. Mech Mater 41:729–741. https://doi.org/10.1016/j.mechmat.2009.01.021
11. Bareither CA, Benson CH, Edil TB (2008) Comparison of shear strength of sand backfills measured in small-scale and large-scale direct shear tests. Can 45:1224–1236
12. Beakawi Al-Hashemi HM, Baghabra Al-Amoudi OS (2018) A review on the angle of repose of granular materials. Powder Technol 330:397–417
13. Bowman ET, Soga K, Drummond W (2001) Particle shape characterisation using Fourier descriptor analysis. Géotechnique 51:545–554. https://doi.org/10.1680/geot.2001.51.6.545
14. Chaney R, Demars K, Santamarina J, Cho G (2001) Determination of critical state parameters in sandy soils—simple procedure. Geotech Test J 24:185. https://doi.org/10.1520/GTJ11338J
15. Cho J, Sohn H (2016) Effects of particle shape and size distribution on the overall fluid-solid reaction rates of particle assemblages. Can J Chem Eng 94:1516–1523. https://doi.org/10.1002/cjce.22533
16. Cleary PW, Sawley ML (2002) DEM modelling of industrial granular flows: 3D case studies and the effect of particle shape on hopper discharge. Appl Math Model 26:89–111. https://doi.org/10.1016/S0307-904X(01)00050-6
17. Cruz-Matías I, Ayala D, Hiller D et al (2019) Sphericity and roundness computation for particles using the extreme vertices model. J Comput Sci 30:28–40. https://doi.org/10.1016/j.jocs.2018.11.005
18. Delaney GW, Cleary PW (2009) Fundamental relations between particle shape and the properties of granular packings. AIP Conf Proc 1145:837–840. https://doi.org/10.1063/1.3180058
19. Fu X, Huckb D, Makeinb L et al (2012) Effect of particle shape and size on flow properties of lactose powders. Particuology 10:203–208. https://doi.org/10.1016/j.partic.2011.11.003
20. Fukunaka T, Sawaguchi K, Golman B, Shinohara K (2005) Effect of particle shape of active pharmaceutical ingredients prepared by

fluidized-bed jet-milling on cohesiveness. J Pharm Sci 94:1004–1012. https://doi.org/10.1002/jps.20307

21. Gardner M, Sitar N (2019) Coupled three-dimensional discrete element-lattice Boltzmann methods for fluid-solid interaction with polyhedral particles. Int J Numer Anal Methods Geomech 43:2270–2287. https://doi.org/10.1002/nag.2972
22. Goudarzy M, König D, Schanz T (2018) Interpretation of small and intermediate strain characteristics of Hostun sand for various stress states. Soils Found. https://doi.org/10.1016/j.sandf.2018.09.002
23. Guida G, Viggiani GMB, Casini F (2020) Multi-scale morphological descriptors from the fractal analysis of particle contour. Acta Geotech 15:1067–1080. https://doi.org/10.1007/s11440-019-00772-3
24. Han J, Wang K, Wang X, Monteiro PJM (2016) 2D image analysis method for evaluating coarse aggregate characteristic and distribution in concrete. Constr Build Mater 127:30–42. https://doi.org/10.1016/j.conbuildmat.2016.09.120
25. Han F, Ganju E, Salgado R, Prezzi M (2018) Effects of interface roughness, particle geometry, and gradation on the sand-steel interface friction angle. J Geotech Geoenviron Eng 144:04018096. https://doi.org/10.1061/(ASCE)GT.1943-5606.0001990
26. Han L, Murphy RF, Ramanan D (2018) Learning generative models of tissue organization with supervised GANs. In: 2018 IEEE winter conference on applications of computer vision
27. He H, Zheng J (2020) Simulations of realistic granular soils in oedometer tests using physics engine. Int J Numer Anal Methods Geomech 44:983–1002. https://doi.org/10.1002/nag.3031
28. Hilton JE, Cleary PW (2011) The influence of particle shape on flow modes in pneumatic conveying. Chem Eng Sci 66:231–240. https://doi.org/10.1016/j.ces.2010.09.034
29. Hogg R, Turek ML, Kaya E (2004) The role of particle shape in size analysis and the evaluation of comminution processes. Part Sci Technol 22:355–366. https://doi.org/10.1080/02726350490516019
30. Hryciw RD, Zheng J, Shetler K (2016) Comparison of particle roundness and sphericity by traditional chart and computer methods. J Geotech Geoenviron Eng 142:04016038. https://doi.org/10.1061/(ASCE)GT.1943-5606.0001485
31. Jerves AX, Kawamoto RY, Andrade JE (2016) Effects of grain morphology on critical state: a computational analysis. Acta Geotech 11:493–503. https://doi.org/10.1007/s11440-015-0422-8
32. Kandasami R, Murthy T (2014) Effect of particle shape on the mechanical response of a granular ensemble. In: Geomechanics from Micro to Macro, pp 1093–1098
33. Kawamoto R, Andò E, Viggiani G, Andrade JE (2018) All you need is shape: predicting shear banding in sand with LS-DEM. J Mech Phys Solids 111:375–392. https://doi.org/10.1016/j.jmps.2017.10.003
34. Krumbein WC (1941) Measurement and geological significance of shape and roundness of sedimentary particles. SEPM J Sediment Res. https://doi.org/10.1306/d42690f3-2b26-11d7-8648000102c1865d
35. Krumbein WC, Sloss LL (1951) Stratigraphy and sedimentation. W.H. Freeman and Company, San Francisco
36. Lai Z, Chen Q (2019) Reconstructing granular particles from X-ray computed tomography using the TWS machine learning tool and the level set method. Acta Geotech 14:1–18. https://doi.org/10.1007/s11440-018-0759-x
37. Lanaro F, Tolppanen P (2002) 3D characterization of coarse aggregates. Eng Geol 65:17–30. https://doi.org/10.1016/S0013-7952(01)00133-8
38. Lashkari A, Falsafizadeh SR, Shourijeh PT, Alipour MJ (2020) Instability of loose sand in constant volume direct simple shear tests in relation to particle shape. Acta Geotech. https://doi.org/10.1007/s11440-019-00909-4
39. Lee C, Suh HS, Yoon B, Yun TS (2017) Particle shape effect on thermal conductivity and shear wave velocity in sands. Acta Geotech 12:615–625. https://doi.org/10.1007/s11440-017-0524-6
40. Li C, Ashlock JC, White DJ et al (2017) Gyratory abrasion with 2D image analysis test method for evaluation of mechanical degradation and changes in morphology and shear strength of compacted granular materials. Constr Build Mater. https://doi.org/10.1016/j.conbuildmat.2017.07.013
41. Lin X, Ng TT (1997) A three-dimensional discrete element model using arrays of ellipsoids. Géotechnique 47:319–329. https://doi.org/10.1680/geot.1997.47.2.319
42. Liu X, Yang J (2018) Shear wave velocity in sand: effect of grain shape. Géotechnique 68:742–748. https://doi.org/10.1680/jgeot.17.t.011
43. Masad E, Olcott D, White T, Tashman L (2001) Correlation of fine aggregate imaging shape indices with asphalt mixture performance. Transp Res Rec J Transp Res Board 1757:148–156. https://doi.org/10.3141/1757-17
44. Masad E, Al-Rousan T, Button J et al (2007) Test methods for characterizing aggregate shape texture, and angularity. Transportation Research Board, Washington, DC
45. Medina DA, Jerves AX (2019) A geometry-based algorithm for cloning real grains 2.0. Granul Matter 21:1–12. https://doi.org/10.1007/s10035-018-0851-9
46. Mehring JL, McBride EF (2007) Origin of modern quartzarenite beach sands in a temperate climate, Florida and Alabama, USA. Sediment Geol 201:432–445. https://doi.org/10.1016/j.sedgeo.2007.07.010
47. Miller NA, Henderson JJ (2011) Correlating particle shape parameters to bulk properties and load stress at two water contents. Agron J 103:1514–1523. https://doi.org/10.2134/agronj2010.0235
48. Mukunoki T, Miyata Y, Mikami K, Shiota E (2016) X-ray CT analysis of pore structure in sand. Solid Earth 7:929–942. https://doi.org/10.5194/se-7-929-2016
49. Nouguier-Lehon C, Cambou B, Vincens E (2003) Influence of particle shape and angularity on the behaviour of granular materials: a numerical analysis. Int J Numer Anal Methods Geomech 27:1207–1226. https://doi.org/10.1002/nag.314
50. Pan T, Tutumluer E, Carpenter SH (2006) Effect of coarse aggregate morphology on permanent deformation behavior of hot mix asphalt. J Transp Eng 132:580–589. https://doi.org/10.1061/(asce)0733-947x(2006)132:7(580)
51. Peralta AF (2016) Identification of optimum aggregate gradation for transportation applications of multiaxial geogrids. Georgia Institute of Technology, Atlanta
52. Pournin L, Weber M, Tsukahara M et al (2005) Three-dimensional distinct element simulation of spherocylinder crystallization. Granul Matter 7:119–126. https://doi.org/10.1007/s10035-004-0188-4
53. Powers MC (1953) A new roundness scale for sedimentary particles. SEPM J Sediment Res. https://doi.org/10.1306/d4269567-2b26-11d7-8648000102c1865d
54. Resentini A, AndÒ S, Garzanti E (2018) Quantifying roundness of detrital minerals by image analysis: sediment transport, shape effects, and provenance implications. J Sediment Res 88:276–289. https://doi.org/10.2110/jsr.2018.12
55. Shin H, Santamarina JC (2013) Role of particle angularity on the mechanical behavior of granular mixtures. J Geotech Geoenviron Eng 139:353–355. https://doi.org/10.1061/(asce)gt.1943-5606.0000768
56. Smith A, Dixon N, Fowmes GJ (2017) Early detection of first-time slope failures using acoustic emission measurements: large-

scale physical modelling. Géotechnique 67:138–152. https://doi.org/10.1680/jgeot.15.P.200
57. Suh HS, Kim KY, Lee J, Yun TS (2017) Quantification of bulk form and angularity of particle with correlation of shear strength and packing density in sands. Eng Geol 220:256–265. https://doi.org/10.1016/j.enggeo.2017.02.015
58. Sukumaran B, Ashmawy AK (2001) Quantitative characterisation of the geometry of discret particles. Géotechnique 51:619–627. https://doi.org/10.1680/geot.2001.51.7.619
59. Sun Q, Zheng J (2019) Two-dimensional and three-dimensional inherent fabric in cross-anisotropic granular soils. Comput Geotech 116:103197. https://doi.org/10.1016/j.compgeo.2019.103197
60. Sun Q, Zheng J, Li C (2019) Improved watershed analysis for segmenting contacting particles of coarse granular soils in volumetric images. Powder Technol 356:295–303. https://doi.org/10.1016/j.powtec.2019.08.028
61. Sun Q, Zheng Y, Li B et al (2019) Three-dimensional particle size and shape characterisation using structural light. Géotech Lett 9:72–78
62. Tutumluer E, Pan T (2008) Aggregate morphology affecting strength and permanent deformation behavior of unbound aggregate materials. J Mater Civ Eng 20:617–627. https://doi.org/10.1061/(asce)0899-1561(2008)20:9(617)
63. Tutumluer E, Pan T, Carpenter SH (2005) Investigation of aggregate shape effects on hot mix performance using an image analysis approach. Transportation Engineering Series No. 137, Federal Highway Administration, Washington, D.C
64. Vangla P, Roy N, Latha GM (2016) Quantification of particle morphology through image based techniques and its importance in forensic studies. In: Proceedings of the 5th International Conference on Forensic Geotechnical Engineering
65. Vangla P, Roy N, Gali ML (2017) Image based shape characterization of granular materials and its effect on kinematics of particle motion. Granul Matter. https://doi.org/10.1007/s10035-017-0776-8
66. Vanimisetti SK, Ramakrishnan N (2012) Effect of the electrode particle shape in Li-ion battery on the mechanical degradation during charge–discharge cycling. J Mech Eng Sci 226:2192–2213
67. Wadell H (1932) Volume, shape, and roundness of rock particles. J Geol 40:443–451. https://doi.org/10.1086/623964
68. Wadell H (1933) Sphericity and roundness of rock particles. J Geol 41:310–331. https://doi.org/10.1086/624040
69. Wadell H (1935) Volume, shape, and roundness of quartz particles. J Geol 43:250–280. https://doi.org/10.1086/624298
70. Wang W, Coop M (2016) An investigation of breakage behaviour of single sand particles using a high-speed microscope camera. Géotechnique 66:984–998. https://doi.org/10.1680/jgeot.15.P.247
71. Wang L, Wang X, Mohammad L, Abadie C (2005) Unified method to quantify aggregate shape angularity and texture using fourier analysis. J Mater Civ Eng 17:498–504. https://doi.org/10.1061/(asce)0899-1561(2005)17:5(498)
72. Wang X, Liang Z, Nie Z, Gong J (2018) Stochastic numerical model of stone-based materials with realistic stone-inclusion features. Constr Build Mater. https://doi.org/10.1016/j.conbuildmat.2018.10.062
73. Wettimuny R, Penumadu D (2004) Application of Fourier analysis to digital imaging for particle shape analysis. J Comput Civ Eng 18:2–9. https://doi.org/10.1061/(asce)0887-3801(2004)18:1(2)
74. Xiao Y, Long L, Matthew Evans T et al (2018) Effect of particle shape on stress-dilatancy responses of medium-dense sands. J Geotech Geoenviron Eng 145:04018105. https://doi.org/10.1061/(asce)gt.1943-5606.0001994
75. Xiao Y, Yuan Z, Lin J et al (2019) Effect of particle shape of glass beads on the strength and deformation of cemented sands. Acta Geotech 14:2123–2131. https://doi.org/10.1007/s11440-019-00830-w
76. Yan B, Regueiro RA (2019) Three-dimensional discrete element method parallel computation of Cauchy stress distribution over granular materials. Int J Numer Anal Methods Geomech 43:974–1004. https://doi.org/10.1002/nag.2917
77. Yang J, Luo XD (2015) Exploring the relationship between critical state and particle shape for granular materials. J Mech Phys Solids 84:196–213. https://doi.org/10.1016/j.jmps.2015.08.001
78. Zhao B, Wang J (2016) 3D quantitative shape analysis on form, roundness, and compactness with μCT. Powder Technol. https://doi.org/10.1016/j.powtec.2015.12.029
79. Zhao S, Zhao J (2019) A poly-superellipsoid-based approach on particle morphology for DEM modeling of granular media. Int J Numer Anal Methods Geomech 43:2147–2169. https://doi.org/10.1002/nag.2951
80. Zheng J, Hryciw RD (2014) Soil particle size characterization by stereophotography. En: Geotechnical Special Publication, pp 64–73
81. Zheng J, Hryciw RD (2015) Traditional soil particle sphericity, roundness and surface roughness by computational geometry. Géotechnique. https://doi.org/10.1680/geot.14.P.192
82. Zheng J, Hryciw RD (2016) Index void ratios of sands from their intrinsic properties. J Geotech Geoenviron Eng 142:1–10. https://doi.org/10.1061/(ASCE)GT.1943-5606.0001575,06016019
83. Zheng J, Hryciw RD (2016) A corner preserving algorithm for realistic DEM soil particle generation. Granul Matter 18:84. https://doi.org/10.1007/s10035-016-0679-0
84. Zheng J, Hryciw RD (2016) Roundness and sphericity of soil particles in assemblies by computational geometry. J Comput Civ Eng 30:1–13. https://doi.org/10.1061/(ASCE)CP.1943-5487.0000578,04016021
85. Zheng J, Hryciw RD (2017) Particulate material fabric characterization by rotational haar wavelet transform. Comput Geotech 88:46–60. https://doi.org/10.1016/j.compgeo.2017.02.021
86. Zheng J, Hryciw RD (2017) Soil particle size and shape distributions by stereophotography and image analysis. Geotech Test J 40:317–328. https://doi.org/10.1520/GTJ20160165
87. Zheng J, Hryciw RD (2018) Cross-anisotropic fabric of sands by wavelet-based simulation of human cognition. Soils Found 58:1028–1041. https://doi.org/10.1016/j.sandf.2018.06.001
88. Zheng J, Hryciw RD, Ohm H-S (2014) Three-dimensional translucent segregation table (3D-TST) test for soil particle size and shape distribution. In: Geomechanics from micro to macro, pp 1037–1042
89. Zheng J, Hryciw RD, Ventola A (2017) Compressibility of sands of various geologic origins at pre-crushing stress levels. Geol Geotech Eng. https://doi.org/10.1007/s10706-017-0225-9
90. Zhou WH, Jing XY, Yin ZY, Geng X (2019) Effects of particle sphericity and initial fabric on the shearing behavior of soil–rough structural interface. Acta Geotech 14:1699–1716. https://doi.org/10.1007/s11440-019-00781-2